Desalination and Water Treatment
www.deswater.com

doi: 10.5004/dwt.2021.26463

211 (2021) 181–195
January

A comparative study on photocatalytic activities of various transition metal oxides nanoparticles synthesized by wet chemical route

Muhammad Farooq Warsi[a,*], Nusrat Shaheen[a], Muhammad Ilyas Sarwar[b], Philips O. Agboola[c], Imran Shakir[d], Sonia Zulfiqar[e,*]

[a]Department of Chemistry, Baghdad-ul-Jadeed Campus, The Islamia University of Bahawalpur, Bahawalpur – 63100, Pakistan, emails: Farooq.warsi@iub.edu.pk (M.F. Warsi), nnshaheennn@gmail.com (N. Shaheen)
[b]Department of Chemistry, Quaid-i-Azam University, Islamabad – 45320, Pakistan, email: ilyassarwar@hotmail.com
[c]College of Engineering Al-Muzahmia Branch, King Saud University, P.O. Box: 800, Riyadh 11421, Saudi Arabia, email: paboola@ksu.edu.sa
[d]Sustainable Energy Technologies (SET) Center, College of Engineering, King Saud University, P.O. Box: 800, Riyadh 11421, Saudi Arabia, email: mshakir@ksu.edu.sa
[e]Department of Chemistry, School of Sciences and Engineering, The American University in Cairo, New Cairo 11835, Egypt, email: sonia.zulfiqar@aucegypt.edu

Received 13 March 2020; Accepted 17 August 2020

ABSTRACT

Co-precipitation route was used to synthesize different oxides of transition metals nano photocatalysts (Fe_2O_3, MnO_2, Co_3O_4, and ZnO). The crystal structure, morphology, and elemental composition confirmation were carried out energy dispersive X-ray spectroscopy through X-ray diffraction (XRD), field emission scanning electron microscopy, and EDXS techniques. XRD analysis results revealed that the transition metal oxides are highly pure and have a very small crystallite size. It was found that iron oxide and cobalt oxide nanostructures were cubic, whereas manganese oxide, and zinc oxide nanostructures have tetragonal crystal structures. Fourier transform infrared spectra were studied to further confirm and clarify the material's structure. Surface areas of the synthesized transition metal oxides nano photocatalysts were calculated through Brunauer–Emmett–Teller isotherms. The calculated optical band gap energy for different metal oxides was between 2.02 and 2.7 eV. The nano photocatalysts were applied in the presence of aqueous methylene blue solution under visible light incandescence in order to set up the ascendancy of heterogeneous photocatalysis. It is observed that the photocatalytic efficiency of the oxides of transition metals simply depends upon the particle size of the nano-sized material and its surface area. It is concluded that iron oxide nano-photocatalyst reveals the best photocatalytic efficiency because of the high surface/charge ratio and variation in surface orientations. It is suggested that nano-sized iron oxides (Fe_2O_3) is a propitious candidate to resolve environmental issues related to the poisonous ecosystem because it has a great potentiality in heterogeneous photo disintegration and can establish a better green environment.

Keywords: Nanoparticles; Surface area; Co-precipitation route; XRD; FTIR; Photocatalysis

---

[*] Corresponding authors.

1944-3994/1944-3986 © 2021 Desalination Publications. All rights reserved.

1. Introduction

Industrial waste comprises a lot of injurious contaminated materials that cause adverse effects on nature. In previous decades, most developing states have faced environmental discomforts due to water, air, and soil contamination with daily basis industrial waste products [1–3]. These growing environmental affairs affected mankind badly in this era of fast-growing population, rapid industrial developments, and climate changes [4,5]. Dye consumption by different industries like fabrics, paper, cosmetics, and leather to color their products contributed a huge amount of dyed wastewater in the environment. Contaminants containing dyes are well known as world ecological deathtraps that play a lead role in marine ecosystem contamination [6]. Waste-water containing the dye is hazardous and highly toxic for natural water sources if it remains untreated. It is mandatory to abolish the dye from water by adopting such a method which is nature friendly [7–9]. These environmental troubles have necessitated the requirement to disintegrate the hazardous products from environment to facilitate human health and to save ecosystem [10,11]. Various approaches have been practiced to discard these impurities from the system [12]. Among all relevant techniques, heterogeneous photocatalysis is the most appropriate one [13]. The reason to apply this method is the achievement of best degradation efficiency and mineralization of the pollutants at room temperature [14,15]. During photocatalytic experiment, a photocatalyst can lost its performance due to reunion of charge carriers produced during photoreaction. This must cause hindrance in photocatalytic efficiency and reduce its application in the recovery environmental issues. It is mandatory to tune photocatalyst performance by reducing its bandgap energy and particle size and enhancing its surface area to cope recombination. A lot of schemes are developed to prepare such materials which assist to overcome environmental problems and assist to clean ecosystem [16–20].

Nano-sized materials have foreground significance due to their magnificent characteristics and promising applications in several fields [21–23]. The discrete and outstanding characteristics of the nano-sized materials comparative to their bulk component make them fruitful in various fields of science and technology [24,25]. Among different nano-sized materials, oxides of transition metals are appealing candidates for photocatalytic applications because of their high stability under ultraviolet light, low cost, high resistivity toward corrosion, and their relative abundances [26,27]. Transition metals exhibiting vacant *d*-orbital are capable of losing electron which make them good semiconductor material [28]. Semiconductors of transition metal oxide nanoparticles like ZnO [29], Co_2O_3 [30], TiO_2 [31,32], MnO_2 [33], Fe_2O_3 [34], AgO [35], NiO [36], and CuO [37] exhibit amazing characteristics such as high chemical stability, friendly to ecosystem, wide range of band gap energies, good catalytic activity, and high surface area [22]. Iron oxide (Fe_2O_3) is important among these oxides because of its attractive band gap energy and it is also suitable for oxidative environment due to its high chemical stability [38,39]. Cobalt oxides (Co_3O_4) seek attention and applicable for heterogeneous photocatalysis because these are eco-friendly and highly resistant toward corrosion and oxidation [40]. Zinc oxide (ZnO) is influential for photo-degradation because it has wide band gap, high photosensitive, non-toxic, and cost-effective material [41,42]. The feasibility of manganese dioxide (MnO_2) for photocatalytic activity is due to its large surface area, corrosion free nature, and resistant to oxidation [43].

In this research work, we synthesized different types of simple oxides of transition metals as nano photocatalyst, and their photocatalytic efficiency was studied briefly. A comparison between band gap energies of different simple oxides of transition metals has also been drawn to examine their photocatalytic efficiencies. Methylene blue (MB) was used as a dye in all photocatalytic experiments.

2. Experimental section

2.1. Materials

Ferrous chloride ($FeCl_2$, 98%), ferric chloride ($FeCl_3$, 98%), zinc nitrate ($ZnNO_3$, 98%), ammonium hydroxide (NH_4OH, 99%), and fumaric acid ($C_4H_4O_4$, 99%) were purchased from Sigma-Aldrich (Europe). Sodium hydroxide (NaOH, 99%), potassium per manganite ($KMnO_4$, 99%), and hydrochloric acid (HCl, 37%) were purchased from Riedel-deHaen (Hong Kong). Sulfuric acid (H_2SO_4, 95.98%) and hydrogen peroxide (H_2O_2, 35%) were purchased from Merck (Germany). Cobalt nitrate ($Co(NO_3)_2 \cdot 6H_2O$, 99%) and ammonium carbonate ($(NH_4)_2CO_3$, 85%) were acquired from Analar. Analytical grade chemicals without any purification were consumed in all preparation routes.

2.2. Synthesis of Fe_2O_3, MnO_2, Co_3O_4, and ZnO

To synthesize Fe_2O_3, 1 mole of $FeCl_2$ and 2 moles of $FeCl_3$ were taken individually. Two moles of HCl were added in each solid. The two solutions were mixed together. The stirring was continuously done using hot plate. Two molar solution of ammonia was added drop by drop under constant stirring for about 2–3 h to adjust pH 9.8. Brown color precipitates were received which were washed with deionized water and ethanol. Drying was done overnight at 70°C [44].

Synthesis of manganese oxide was done by the redox reaction between $KMnO_4$ and fumaric acid. 7.6 g and 1.4 g of $KMnO_4$ and fumaric acid were taken, respectively. 2.5 M (4 mL) sulfuric acid was poured along with 100 mL distilled water into the above mixture. pH 5 was adjusted using ammonium carbonate solution. Color of the reacting mixture changed from purple to orange and brown colored suspension was obtained after 25–30 min. One hundred degree Celsius drying and 450°C calcination was done for 5 h. The reaction route was supervised for color changes of reaction mixture starting from purple to orange and then brown. Vanishing of the purple color of supernatant liquid is the indication of $KMnO_4$ complete reducion [45].

To prepare cobalt oxide (Co_3O_4), 0.5 mol (20 mL) cobalt nitrate was added in freshly prepared 0.25 mol (80 mL) sodium hydroxide solution under continuous stirring. On addition, blue colored solution was obtained which slowly turned pink. Thirty percent of (0.5 mL) hydrogen peroxide solution was added in pink suspension under vigorous stirring which yield brown colored precipitates. The change in color is the indication of conversion of Co^{2+} to Co^{3+}. The reacting solution was placed in water bath for 5 h at 90°C to get black precipitates. The precipitates were filtered, washed three to four times, dried for 3–4 h for 60°C–70°C [46]. The growth mechanism of Co_3O_4 can be summarized by the given equations:

$$Co(NO_3)_2 + NaOH \rightarrow Co(OH)NO_3 + NaNO_3 \quad (1)$$

$$Co(OH)NO_3 + NaOH \rightarrow Co(OH)_2 + NaNO_3 \quad (2)$$

$$4Co(OH)_2 + O_2 + H_2O \rightarrow 4Co(OH)_3 \quad (3)$$

$$3Co(OH)_3 + 1/2O_2 \rightarrow Co_3O_4 + 6H_2O \quad (4)$$

Zinc oxide was prepared using zinc nitrate ($Zn(NO_3)_2$ and ammonium carbonate $(NH_4)_2CO_3$ precursors using 1:1.5 mol ratio. 1 M zinc nitrate and 1.5 M ammonium carbonate solutions were prepared. The two solutions were mixed under continuous stirring for 5 min. The obtained precipitates were white in color which were washed, dried at 100°C for 2–2.5 h, and annealed at 300°C for 4 h [47]. Schematic illustration for general co-precipitation route is shown in Fig. 1.

2.3. Characterizations

Morphology and structure determination of the prepared oxides have been carried out with ZEISS LEO SUPRA 55 field emission scanning electron microscopy (FE-SEM) and Philips X'pert PRO 3040/60 diffractrometer, respectively. Elemental composition was confirmed through JEOL JCM-6000Plus SEM. Specific surface area, particle size, and porosity of the prepared oxides were calculated through Brunauer–Emmett–Teller (BET) method at 77 K through N_2 adsorption isotherms using micromeritics ASAP 2020 physisorption analyzer. To further clarify the structure Fourier transform infrared (FTIR) was studied using Tensor 27 spectrometer. Optical studies were characterized through carry 60 UV-visible-NIR dual-beam spectrophotometer.

3. Results and discussion

3.1. Morphology and structure identification

3.1.1. Field emission scanning electron microscopy

Morphological visualization of Fe_2O_3, MnO_2, Co_3O_4, and ZnO were determined using FE-SEM and their FE-SEM micrographs are shown in Figs. 2a–e, respectively. The FE-SEM images for Fe_2O_3, MnO_2, and Co_3O_4 in Figs. 2a–c, respectively, were observed at high magnification while FESEM results for ZnO shown in Figs. 2d and e were noticed at both low and high magnification respectively. The morphology of Fe_2O_3, MnO_2, and Co_3O_4 revealed agglomeration of homogeneous nanoparticles. Zinc oxide (ZnO) FE-SEM results observed at 1 μm and 200 nm show different morphology as compared to the other three oxides. It indicated the formation of nanoclusters having different sizes.

3.1.2. Energy dispersive X-ray spectroscopy

EDXS was also carried out to confirm elemental compositions of the prepared different samples and their spectra are displayed in Figs. 3a–d for Fe_2O_3, MnO_2, Co_3O_4, and ZnO, respectively. EDXS spectrum of Fe_2O_3 in Fig. 3a clearly shows the presence of Fe and O elements. In Fig. 3b, MnO_2 EDXS spectrum can be visualized which shows the

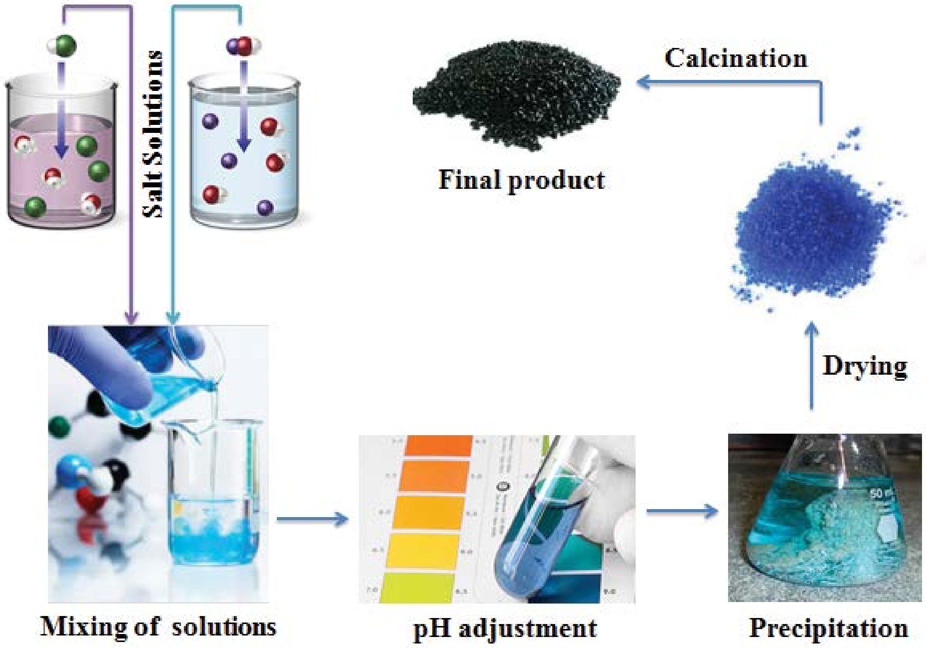

Fig. 1. Schematic illustration of co-precipitation route to synthesize different oxides.

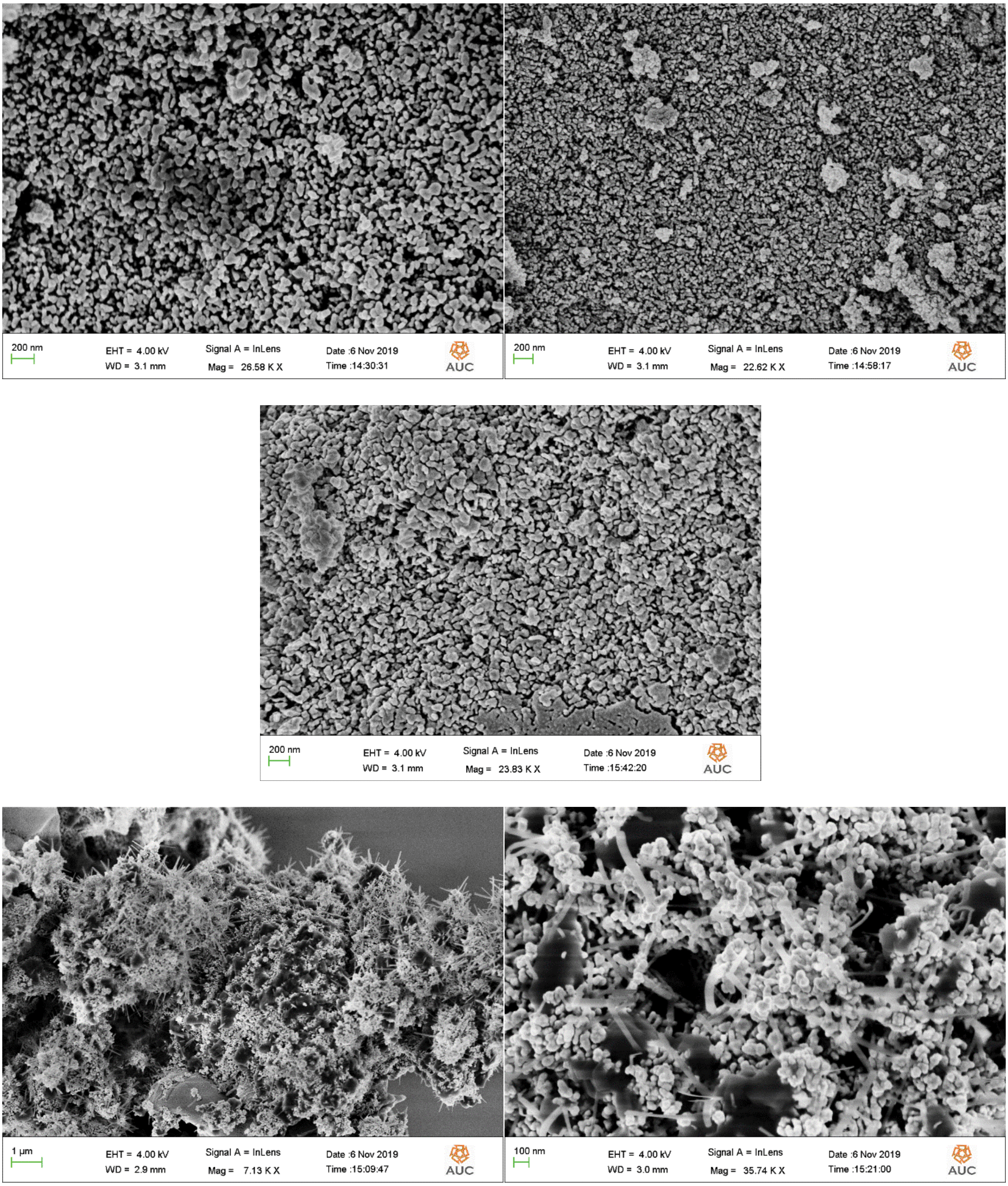

Fig. 2. FE-SEM micrographs for (a) Fe_2O_3, (b) MnO_2, (c) Co_3O_4, (d and e) ZnO nanoparticles.

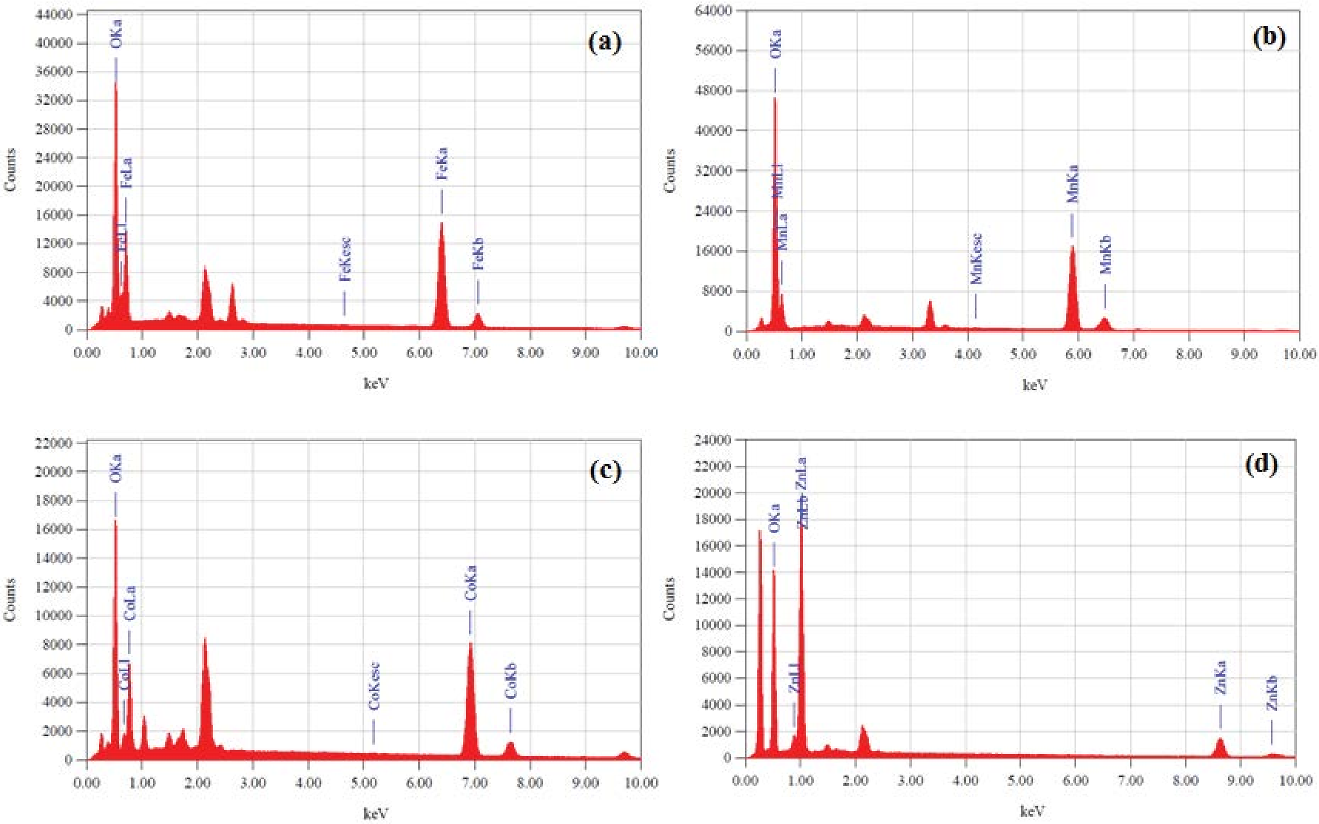

Fig. 3. Energy dispersive X-ray spectra of (a) Fe_2O_3, (b) MnO_2, (c) Co_3O_4, and (d) ZnO nanoparticles.

exclusive presence of Mn and O elements. Similarly in Figs. 3c and d, EDXS spectra of Co_3O_4 and ZnO are given which clearly show the existence of Co and O elements for Co_3O_4 and Zn and O elements for ZnO, respectively. The presence of any additional element is negligible in all the four EDXS spectra which confirm a lack of impurity in four samples.

3.1.3. X-ray diffraction

CuK radiations between 2θ range 20°–80° were used to identify structure and to investigate crystalline nature of the material. Fig. 4a reveals XRD pattern of iron oxide nanoparticles. A wide range of diffraction peaks were noticed having diffraction planes [210], [211], [220], [310], [311], [222], [400], [330], [421], [422], [511], [440], [442], [661], [540], [622], and [444] at 2θ locations 24.06°, 28.17°, 30.23°, 33.01°, 35.5°, 43.42°, 46.20°, 50.46°, 53.82°, 57.06°, 62.78°, 65.56°, 67.91°, 69.81°, 72.01°, 74.51°, 74.51°, and 79.06°. All resultant peaks agree with the reported pattern [JCDPS: 039-1346]. No additional peak and exceptional phases were noticed in the diffraction pattern of γ-Fe_3O_4 which is clear evidence of high purity cubic crystal phase of the sample [48]. Fig. 4b displays diffraction pattern of manganese oxide (MnO_2) in which a lot of diffraction angles at 26.03°, 28.57°, 36.50°, 37.50°, 42.00°, 46.93°, 49.78°, 52.14°, 55.62°, 56.47°, 60.07°, 65.29°, 69.51°, 72.86°, 77.07°, and 78.69° were attributed to [220], [310], [400], [211], [301], [321], [411], [440], [600], [501], [521], [002], [541], [312], [402], and [332] diffraction planes. The values were confirmed from standard values via [JCPDS 44-0141]. The diffraction figure revealed MnO_2 α-phase lattice structure having tetragonal crystal system [49]. There is absence of any peak related to impurity in the diffraction figure of α-MnO_2 which revealed high purity product of the α-phase tetragonal crystal system.

Fig. 4c represents the diffraction specimen of cobalt oxide nanostructures. In the synthetic procedure of Co_3O_4, participation of hydroxyl ions (OH^-) is important. Conversion of Co^{2+} to Co_3O_4 is especially influenced by these ions. Crystallinity of the material is also affected by the presence of OH^-. The diffraction bands observed at 2θ = 36.81°, 38.87°, 44.00°, 49.59°, 55.57°, 59.10°, 65.56°, 68.84°, 74.32°, and 77.98° were related to [220], [311], [222], [400], [331], [422], [511], [440], [531], [620], and [533] lattice planes correspond to the cubic phase of the material [ICDD card number 42-1467]. There were some sharp bands located at 33.03°, 51.18°, 56.67°, 61.04°, 67.26°, 71.16°, and 72.87° denoted diffraction planes [100], [102], [110], [111], [200], [201], and [112] which point out β-$Co(OH)_2$ in the prepared Co_3O_4 [ICDD 30-0443]. Some more peaks were also examined at planes [006], [104], and [009] having 41.68°, 45.82°, and 62.26° 2θ values allocated to CoOOH which are notice via [ICDD card number 07-0169] [46].

Fig. 4d reveals the pattern of zinc oxide (ZnO) powder. The ZnO powder have hexagonal structure with high purity proved from notified peaks at 31.74°, 34.45°, 36.21°, 47.58°, 56.65°, 62.74°, 68.01°, and 69.24° attributed to [100], [002], [101], [102], [110], [103], [112], and [201] with card

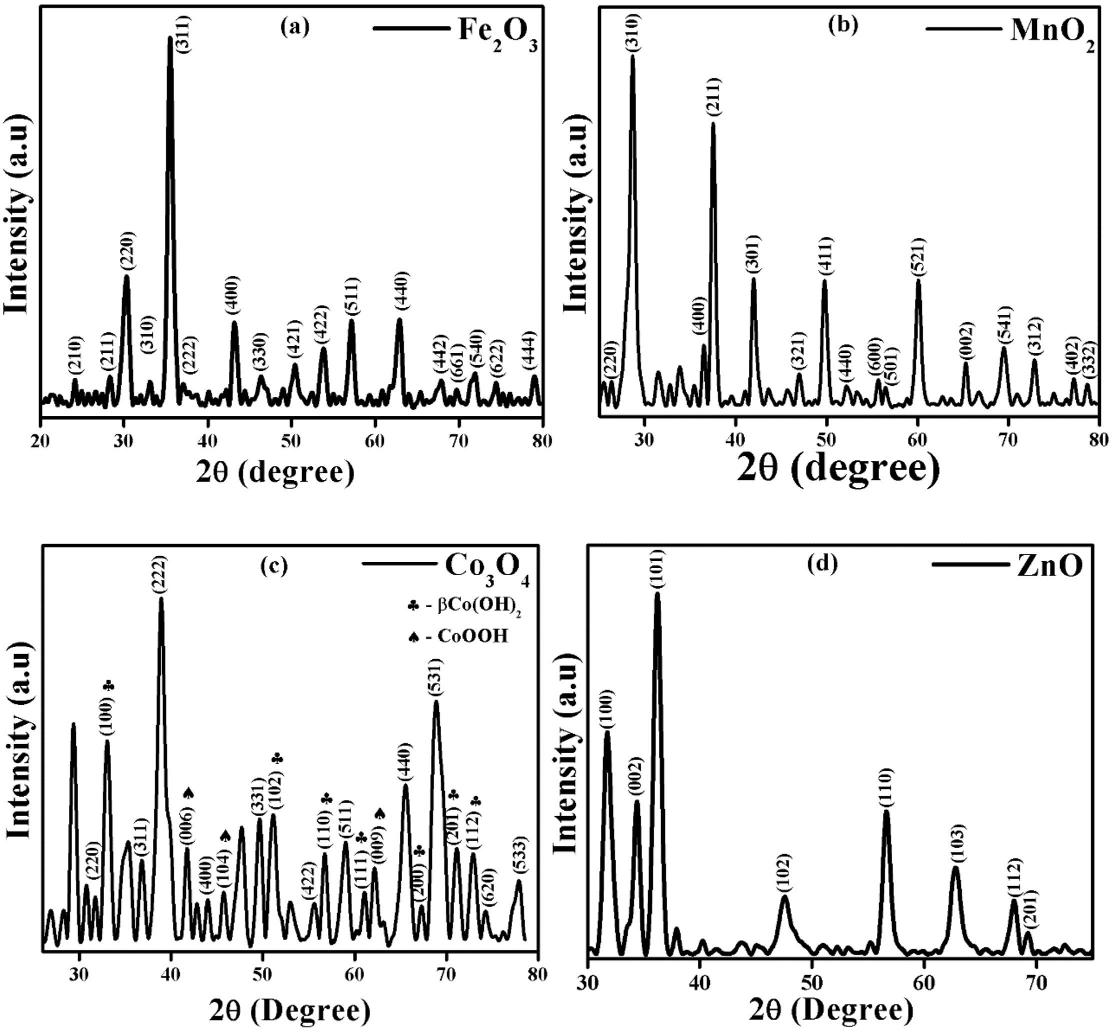

Fig. 4. (a) XRD pattern of Fe_2O_3, (b) XRD pattern of MnO_2, (c) XRD pattern of Co_3O_4, and (d) XRD pattern of ZnO nanoparticles.

number (JCDPS: 036-1451). The absence of any additional peak denoted highly purified product [50].

The crystallite sizes of the samples were calculated by Debye–Scherrer expression [51]. The values of crystallite size and other physical parameters are given in Table 1.

$$D = \frac{k\lambda}{\beta\cos\theta} \tag{5}$$

In Eq. (5), D is the crystallite size, k is the Scherrer constant exhibiting value 0.9, λ is the wavelength of X-rays which is used in the experiment (Cuα = 1.5406 Å), β is the full width at half maximum representing full width and half maximum, and θ is the Bragg's angle. The calculated crystallite sizes for Fe_2O_3 was 14.5 nm, for MnO_2 was 20.77 nm, for Co_3O_4 was 16.4 nm, and for ZnO was 11.7 nm.

The crystallite size of the synthesized samples can also be calculated using Williamson Hall sing equation [52]:

$$\beta_{hkl} = \beta_D + \beta_S \tag{6}$$

$$\beta\cos\theta = \frac{K\lambda}{D} + 4\varepsilon\sin\theta \tag{7}$$

and,

$$\beta_D = \frac{K\lambda}{D\cos\theta}, \quad \beta_S = C_\varepsilon \tan\theta \tag{8}$$

Crystallite size and strain were obtained by the values of intercept and strain from straight-line graph which is plotted between 4sinθ against x-axis and βcosθ against y-axis.

The lattice parameters for cubic crystal system were determined through Eq. (9):

$$a = d\,(h^2 + k^2 + l^2)^{1/2} \tag{9}$$

The lattice parameter for tetragonal system measured through given expressions, respectively.

$$a = d\,[h^2 + k^2 + l^2\,(a/c)^2]^{1/2} \tag{10}$$

3.2. FTIR analysis

FTIR spectroscopy was carried out to further confirm the structure of the materials. The presence of absorbed functional groups on the particles' surface during the synthetic mechanism was also identified by this technique. Tensor 27 spectrometer was used for the experiment. Fig. 5 represents the FTIR spectrum of Fe_2O_3, MnO_2, Co_3O_4, and ZnO nanostructures. The indication of Fe–O bond and existence of hematite (γ-Fe_2O_3) was proved by two strong absorption bands located between 225 and 550 cm^{-1}. The band at 425 cm^{-1} was attributed to Fe–O stretching mode at octahedral void while the band at 536 cm^{-1} was allocated to Fe–O stretching mode at both tetrahedral and octahedral voids. All bands in FTIR spectrum of Fe_2O_3 oxides are related to metal–oxygen bonds whereas no exceptional band is observed which demonstrates impurity free oxide. There was a vibration at 1,615 cm^{-1} due to moisture adsorption in the sample [53–57]. In MnO_2 spectrum, the presence of manganese oxide was identified by the two stretching modes of O–Mn–O found from 470 to 620 cm^{-1} range. Two additional bands were placed at 1,387 and 1,594 cm^{-1} believed to the shadow of OH^- vibrational modes [58,59].

Cobalt oxide FTIR spectrum exhibited two clear modes of vibration (550–660 cm^{-1}) claim the Co–O bond of Co_3O_4. The one present at 550 cm^{-1} designated to Co^{+3} octahedral coordination and the other placed at 654 cm^{-1} specified Co^{+2} tetrahedral coordination [60,61]. FTIR spectrum of ZnO powder gave the peaks obtained (430–520 cm^{-1}) the clear gesture of pure zinc oxide stretching bands. The signals received at 1,430 cm^{-1} were responsible for the vibrations of C=C and dictated the presence of some organic impurity [62–64].

3.3. BET surface area analysis

BET analysis was used to get surface areas of the prepared oxides. The samples were characterized through N_2 adsorption/desorption isotherms at 77 K. Figs. 6a–d show the adsorption/desorption isotherms of Fe_2O_3, MnO_2, Co_3O_4, and ZnO, respectively. It was noticed from the isotherm curves for all the prepared oxides that the hysteresis loop lies in about 0.6–1.0 of relative pressure ($P/P°$). This is the indication of mesoporous character of the prepared oxides. The values for different surface parameters, that is, surface areas, pore volumes, particle sizes, and pore sizes are given in Table 2. The surface area values for different samples obtained from BET data are 56.13, 42.08, 36.45, and 21.72 m^2/g for Fe_2O_3, MnO_2, Co_3O_4, and ZnO, respectively. Whereas, the calculated particle size is 106.89 nm for Fe_2O_3, 142.58 nm for MnO_2, 164.60 nm for Co_3O_4, and 276.25 nm for ZnO. Surface area and particle size of a sample are key components for photocatalytic application. Small particle size provides wide band gap energy to the sample and largest surface area may be responsible for providing additional active sites on the surface of the photocatalyst and favors redox reactions positively. It was noted from surface area values and calculated particle size from BET isotherms that iron oxide (Fe_2O_3) possessed highest surface area and lowest particle size among the prepared four oxides. Zinc oxide (ZnO) has lowest value of surface area and highest particle size among these four oxides. These two factors may probably helpful in determination of the photodegradation potency of the photocatalyst.

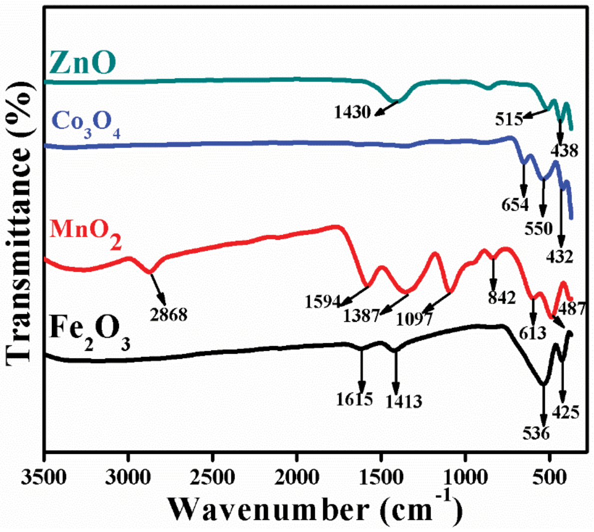

Fig. 5. FTIR spectra of Fe_2O_3, MnO_2, Co_3O_4, and ZnO nanoparticles.

3.4. Optical band gap analysis

Electronic transitions occur within atom and molecules can be investigated through UV/visible spectroscopy. All the samples were analyzed from 200 to 800 nm UV-visible range. Dual-beam Cary 60 UV-visible-NIR spectrophotometer was used to carry out optical analysis. Fig. 7a displays absorption spectrum of iron oxide (Fe_2O_3) in which absorption was noticed at about 376 nm which explains charge transfer through direct transition from ligand to metal. Absorption spectrum of manganese oxide (MnO_2) is presented in Fig. 7b. MnO_2 possess UV-visible broad absorption range 250–500 nm. MnO_2 showed absorption bands at 242 and 417 nm. In MnO_2 visible light absorption occurs due to Mn-ions *d–d* transitions. Splitting of 3D energy states of Mn into lower (t_{2g}) energy state and higher (e_g) energy state occur in ligand manganese oxide octahedra. Optical band gap energy is due to this energy difference in e_g and t_{2g} levels [65,66]. Cobalt oxide (Co_3O_4) spectrum shows in Fig. 7c in which two sharp bands at 229 and 279 nm was noticed which is related to charge transfer of ligand–metal in the product. Fig. 7d exhibits zinc oxide absorption spectrum in which a band situated at 372 nm. Zinc oxide absorption for intrinsic band gap is due to this band. This is due to electronic transitions from O_{2p} to Zn_{3d} from valance to conduction band. Furthermore, it is indicated that the particle size is in nano range and the size distribution is also narrow [67].

Band gap energy of a material is its capability to excite and generate electron and hole pairs for a redox reaction to proceed. It is strongly dependent on the dimensions, size, and shape of the material. The tauc equation for band gap energy calculation is as follows [68]:

$$(\alpha h\nu)^n = A(h\nu - E_g) \tag{11}$$

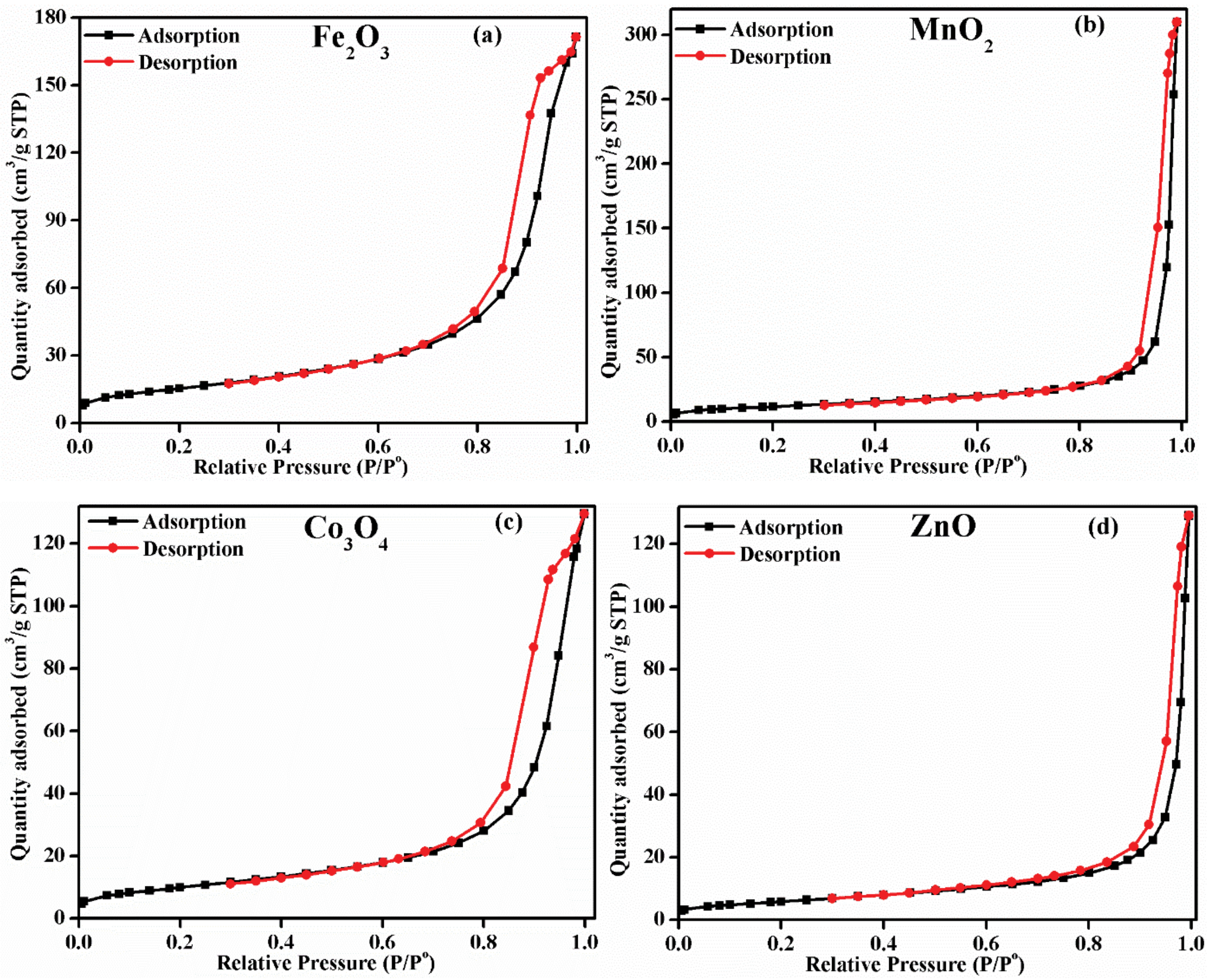

Fig. 6. Adsorption/desorption isotherm curves for (a) Fe_2O_3, (b) MnO_2, (c) Co_3O_4, and (d) ZnO.

Table 1
XRD parameters of different transition metal oxides (Fe_2O_3, MnO_2, Co_3O_4, and ZnO)

Sr. No.	Sample name	Crystal system	Crystallite size (nm)	W. H. plot crystallite size (nm)	Strain	Lattice parameters	
						a (Å)	*c* (Å)
1	Fe_2O_3	Cubic	14.5	10	2.4×10^{-3}	8.8422	–
2	MnO_2	Tetragonal	20.77	12	2.37×10^{-3}	9.8649	2.8540
3	Co_3O_4	Cubic	14.93	16.4	9.9×10^{-4}	9.5280	–
4	ZnO	Tetragonal	11.76	10.67	1.46×10^{-3}	2.6365	5.2213

Table 2
Surface parameters of various transition metal oxides (Fe_2O_3, MnO_2, Co_3O_4, and ZnO)

Sr. No.	Sample name	Surface area (m^2/g)	Particle size (nm)	Pore volume (cm^3/g)	Pore size (nm)
1	Fe_2O_3	56.13	106.89	0.26	18.09
2	MnO_2	42.08	142.58	0.4	37.31
3	Co_3O_4	36.45	164.60	0.2	21.99
4	ZnO	21.72	276.25	0.16	29.26

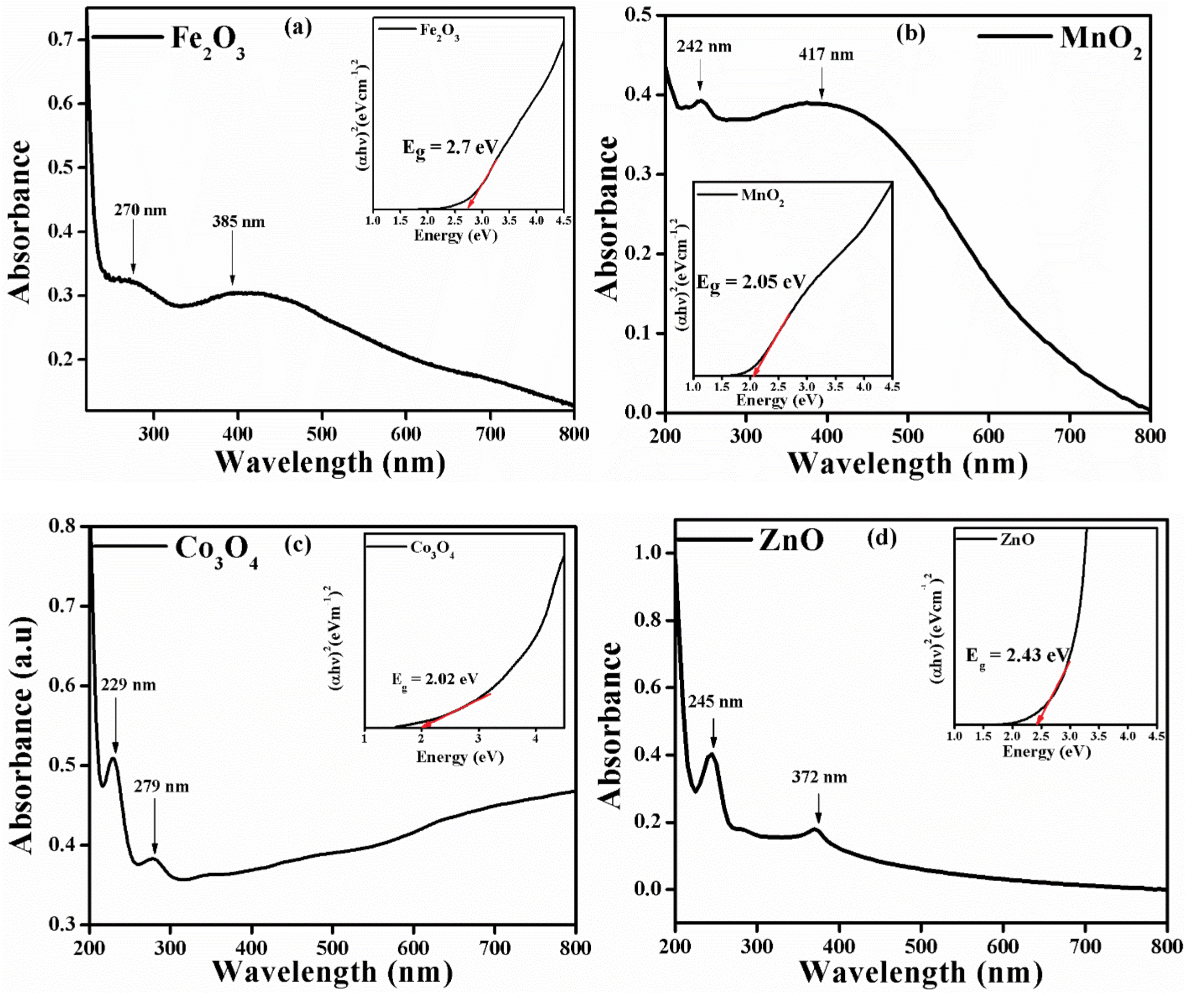

Fig. 7. UV/VIS spectra and tauc plots of (a) Fe_2O_3, (b) MnO_2, (c) Co_3O_4, and (d) ZnO nanoparticles.

where α is the absorption coefficient, h is the plank's constant, ν is the light energy, A is the characteristic constant of the material, E_g is the band gap energy, and n is the constant which is dependent on the nature of electronic transitions. It might be equal to 2 or ½ for direct and indirect transitions of the materials respectively. To find out the band gap energy of the material in eV, a graph between $(\alpha h\nu)^2$ and $h\nu$ on y-axis and x-axis, respectively, is plotted. The curve received from the graph is extrapolated from straight path towards its energy axis and gets the band gap value [69–71]. Tauc plots of Fe_3O_4, MnO_2, Co_3O_4, and ZnO is shown in Figs. 7a–d, respectively. The band gap energies for Fe_3O_4, MnO_2, Co_3O_4, and ZnO were 2.7, 2.05, 2.02, and 2.5 eV, respectively. Greater band gap energy enlarges the space between valance and conduction bands and provides assistance to avoid reunion of electron and hole pairs. This factor may be favorable for oxidation and reduction reactions onto the photocatalyst surface.

3.5. Photocatalytic efficiency

Some key factors which perform significant role in any photo-degradation reaction, that is, the intensity of incident light, pollutant's initial concentration, and concentration of the photocatalyst [1]. There are two main approaches which are important during photocatalytic experiments in the presence of transition metal ions (a) the effect of transition metal ions on the reaction rate of photocatalysis, (b) the conversion of metal ions into relatively less toxic species or the deposition of ions on catalyst surface to recover the expensive and useful metal ions [72]. Transition metal oxide semiconductor nano-photocatalysts are a good choice to remove pollutant dyes because these have less optical band gaps, low cost, and non-toxic nature [33]. Transition metal oxide nano-photocatalysts are also important because these show variations in photocatalytic efficiencies due to crystallographic surface orientations [27].

Photocatalysis experiment was performed for all synthesized samples of transition metal oxide nanoparticles. Methylene blue (MB), an organic dye was used to monitor the performance of photocatalysts. Fifty milliliters of 5 ppm MB solution and 2 mg of catalyst were dissolved. The solution was placed in dark to maintain adsorption–desorption equilibrium at room temperature. Halogen lamp was used as a light source and the sample was placed at a distance of 25 cm from the lamp. The decrement in the rate of absorption was examined by carry 60 UV-visible spectrophotometer after specific intervals of time (0, 10, 20, 30, 40 … 100, 110 min). The degradation percentage of methylene blue was determined by the Eq. (9):

$$\% \text{ degradation } = \eta = \left[1 - \frac{C_0}{C_t}\right] \times 100 \tag{12}$$

Fig. 8 shows photo-degradation of metal oxides (Fe_2O_3, MnO_2, Co_3O_4, and ZnO). The specific absorption peaks observed at about 664 nm in different spectra of transition metal oxides is simply related to MB. The intensities of peaks reduced and new bonds arrived at relative short intensities of organic dye with the passage of time period. The downward shifting of intensities of peaks for different oxides can be clearly observed in the absorption spectra shown in Fig. 8a–d. The characteristic color of organic dye (MB) was disappeared along with time. Transparent color of methylene blue is the indication of complete degradation of dye. Typically, the photo nanocatalyst dye degradation potency of material is related to the capability to generate charge carrier species and vigorous oxidizing agents ($^•O_2^-$ and $^•OH$) that can experience or undergo secondary reactions [73]. General mechanism of photocatalytic activity under transition metal nano-photocatalyst can be observed in Fig. 9. Generally, the reactions occurred during the photocatalysis experiment of transition metal oxide can be enlightened by following mechanism:

$$\text{Transition metal oxides} + h\nu \rightarrow e^-_{(CB)} + h^+_{(VB)} \tag{13}$$

$$h^+_{(VB)} + H_2O \rightarrow H^+ + {}^•OH \tag{14}$$

$$e^-_{(CB)} + O_2 \rightarrow {}^•O_2^- \tag{15}$$

$$h^+_{(CB)} + OH^- \rightarrow {}^•OH \tag{16}$$

$${}^•OH + \text{MB (dye)} \rightarrow CO_2 + H_2O \text{ (degradation products)} \tag{17}$$

$${}^•O_2^- + \text{MB (dye)} \rightarrow CO_2 + H_2O \text{ (degradation products)} \tag{18}$$

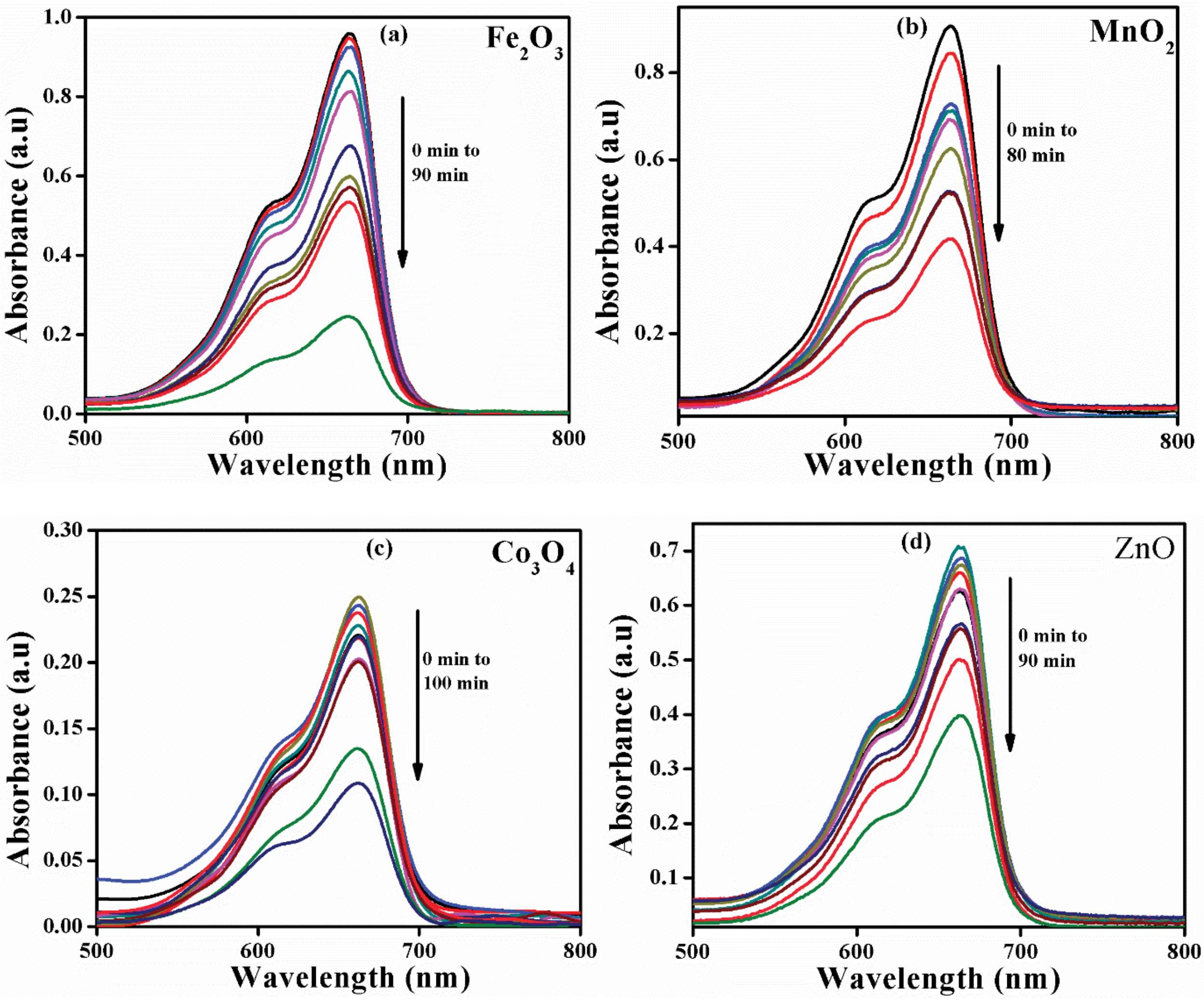

Fig. 8. Photocatalytic behavior of MB using (a) Fe_2O_3 nanocatalyst, (b) MnO_2 nanocatalyst, (c) Co_3O_4 nanocatalyst, and (d) ZnO nanocatalyst at different irradiation time under UV/VIS irradiation.

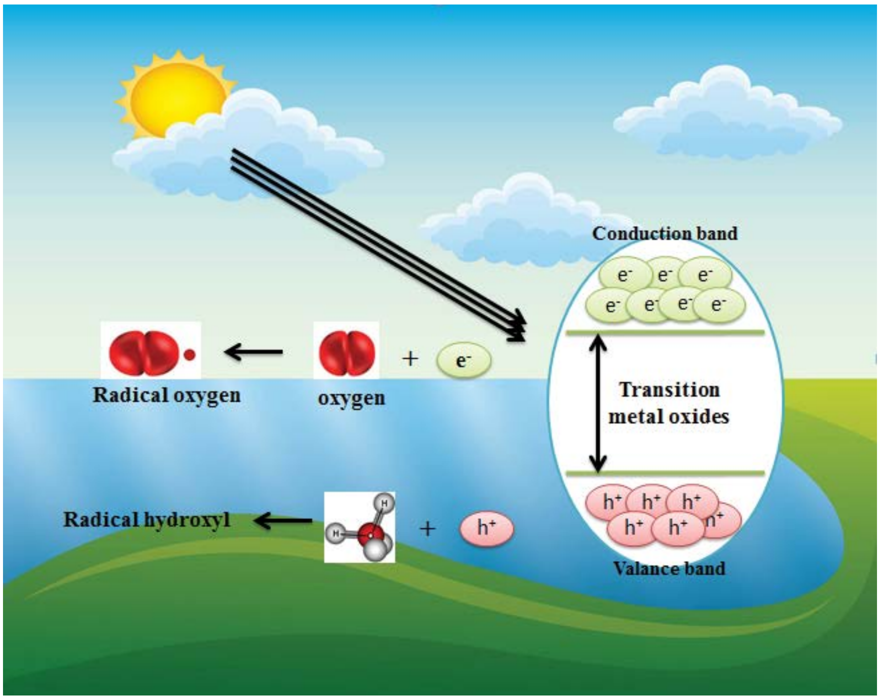

Fig. 9. General mechanism of photo degradation process.

Photcatalytic activities of the transition metal oxides depend upon the generation of excitons on ultraviolet visible light exposure. As photo nanocatalyst exposed to UV-VIS light electrons from VB are excited to CB and generation of electron and hole pairs started [Eq. (10)]. The resultant pairs can either interact with other molecules or recombine. Under adequate circumstances, electron and hole pairs at CB and VB, respectively, travel toward the photocatalyst surface which directly interacts with the solution of dye, to precede oxidation reduction reactions [74].

It is noticed that the materials owing large band gap energy and small surface/charge ratios are more susceptible to excitation upon ultraviolet visible irradiation and recombination rate of photo generated electron and hole pair species is very high [75]. However, the photo-degradation efficiency and reaction rates of model nano-sized photocatalysts are highly dependent upon (i) small particle size, (ii) low optical band gap energy, (iii) greater surface area of nano photocatalyst, (iv) enhanced rate of absorption of light at photocatalyst interface, (v) decrement in reunion rate of charge carrier species at the catalyst surface, and (vi) pH of the nano photocatalyst. Such nano-sized photocatalysts should have better charge carriers' migration capability, charge separation proficiency and appropriate position in valance and conduction bands for oxidation–reduction reactions [75]. Adsorption capability and increase in the light absorption of the nano-sized photocatalyst is probably enhanced by large surface area. Whereas, wide band gap energy is due to relatively small particle size of the photocatalyst. In consequence, charges migration toward the surface and their reunion is limited. The pH is complex and very significant parameter in the photodegradation experiment as it highly affects nanoparticles' electrostatic interactions, the potential band that influences the ability of nano sized particles to effect the oxidation–reduction reactions in the solution and the isoelectric point which impacts the oxides' dispersion. The pH performs key role in the reaction mechanism (attack of hydroxyl radical, direct oxidation, and reduction of positive hole and negative electron in the conduction band respectively. It also affects the dye characteristics. The tested pH for natural and wastewaters ranges from 3 to 11 [76,77]. The mechanism between reactive dye (MB) and nano sized photocatalyst can be proposed as follows [78]:

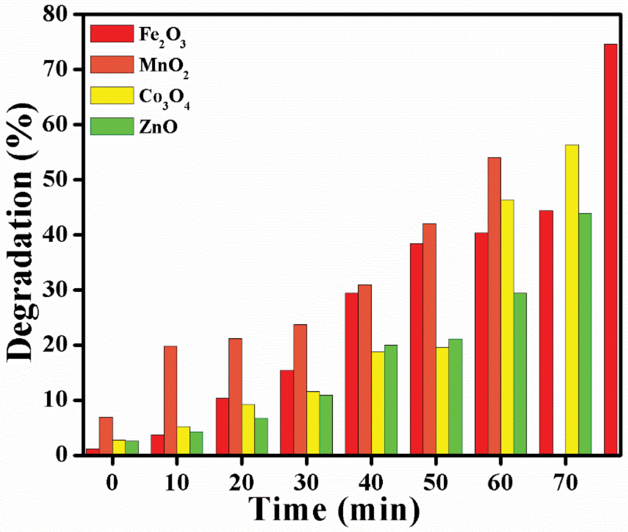

Fig. 10. Percentage degradation rate of MB at specific time intervals under different nano photocatalyst.

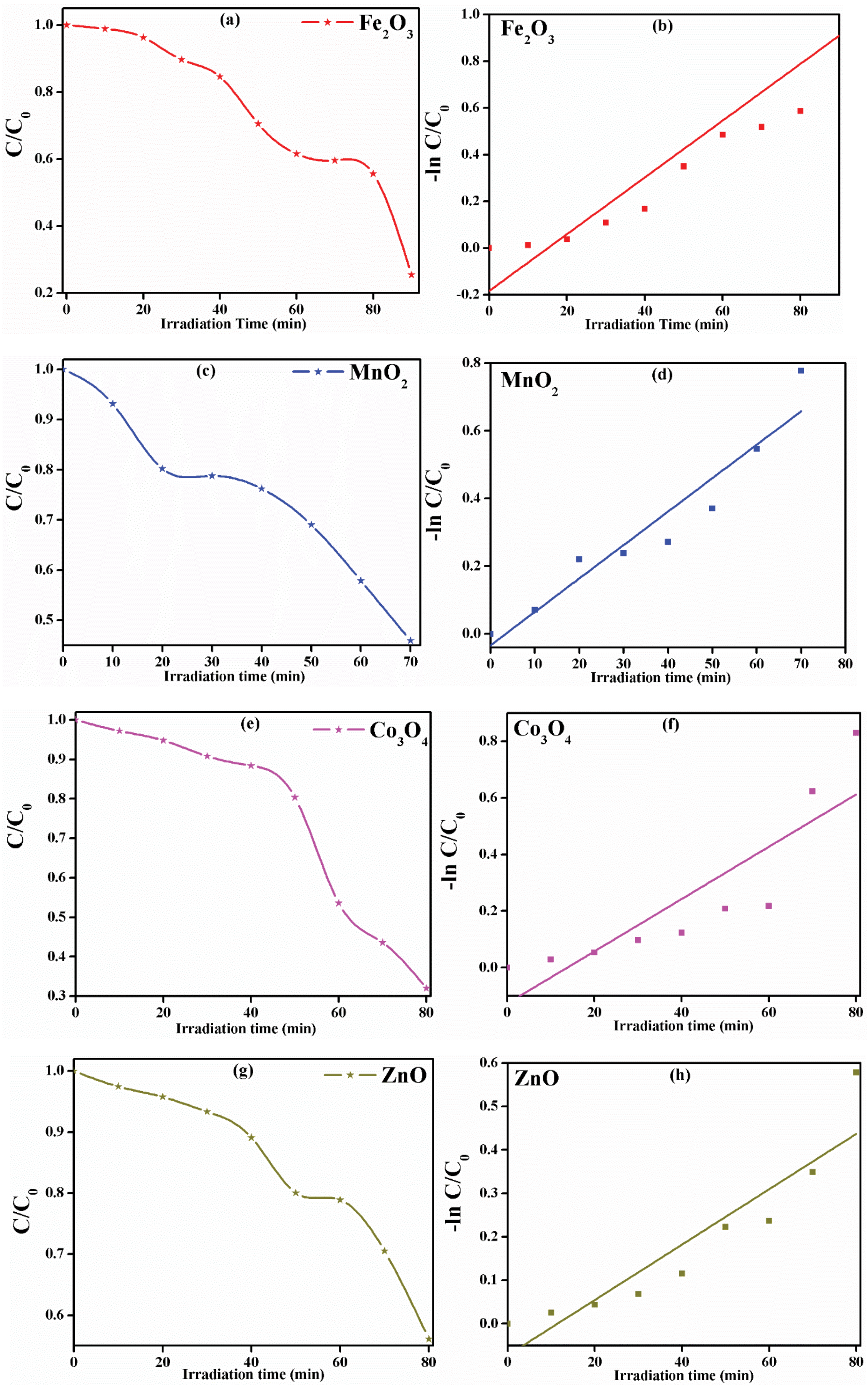

Fig. 11. Photocatalytic degradation profile under UV/VIS irradiation. (a) Kinetics of Fe_2O_3 nanocatalyst, (b) $-\ln C/C_0$ vs. time of Fe_2O_3 nanocatalyst, (c) kinetics of MnO_2 nanocatalyst, (d) $-\ln C/C_0$ vs. time of MnO_2 nanocatalyst, (e) kinetics of Co_3O_4 nanocatalyst, (f) $-\ln C/C_0$ vs. time of Co_3O_4 nanocatalyst, (g) kinetics of ZnO nanocatalyst, and (h) $-\ln C/C_0$ vs. time of ZnO nanocatalyst.

Table 3
Degradation percentage and rate constant (min^{-1}) values of different transition metal oxides (Fe_2O_3, MnO_2, Co_3O_4, and ZnO)

Sr. No.	Sample name	Degradation (%)	Rate constant (min^{-1})
1	Fe_2O_3	74.58	1.21×10^{-2}
2	MnO_2	54.03	1.0×10^{-2}
3	Co_3O_4	56.40	0.92×10^{-2}
4	ZnO	44	0.64×10^{-2}

$$\text{Nano photocatalyst} + h\nu \rightarrow \text{Nano photocatalyst } (h^+_{VB} + e^-_{CB}) \quad (19)$$

$$\text{MB (dye)} + h^+_{VB} \rightarrow MB^{\bullet +} \text{ (dye oxidation)} \quad (20)$$

or

$$OH^- + h^+_{VB} \rightarrow OH^\bullet \quad (21)$$

$$\text{MB (dye)} + OH^\bullet \rightarrow \text{dye degradation} \quad (22)$$

The degradation rate of nano-photocatalysts of prepared different oxides can be observed in Fig. 10. The reactions occurred during whole experiment follow pseudo-first-order kinetics and their different graphs are plotted in Fig. 11. As photocatalytic degradation reactions follow kinetics of pseudo-first-order reaction so the rate constant values of methylene blue for different nanocatalysts were calculated by pseudo-first-order equation.

$$-\ln\left[\frac{C_t}{C_0}\right] = kt \quad (23)$$

Here C_t and C_0 are the concentrations time at different intervals and initial concentration of dye, t is irradiation time and k is value of rate constant of photodegradation reaction. The value of k can be measured by linear fit the plot of $[\ln C/C_0]$ vs. time in Fig. 11. The % age degradation and rate constant values can be visualized in Table 3. Among the four transition metal oxide samples, the results indicate Fe_2O_3 exhibit highest rate constant value ($k = 1.21 \times 10^{-2}$) and highest degradation potency (74.58%). The hydroxyl radical $OH^\bullet$ is responsible for the high rate constant value which boosts up the degradation procedure effectively.

It is noted by degradation percentages and rate constant values of different transition metal oxides that all the simple oxides have good catalytic activity. Among prepared four samples, iron oxide showed highest degradation rate while cobalt oxide showed least photocatalytic efficiency. It may be suggested that iron oxide nano photocatalyst exhibit best catalytic efficiency and is the promising candidate to remove dangerous trashes from ecosystem vigorously whereas MnO_2, Co_3O_4, and ZnO did not show significant photocatalytic proficiency in contrast to the Fe_2O_3.

4. Conclusion

In aforementioned work, the degradation of methylene blue aqueous solution has been studied under visible light irradiation to monitor the photo degradation ability of the transition metal oxide nano photo catalysts. Examination of photocatalytic efficiencies of the transition metal oxides have been carried out at definite time intervals until the regular blue color of aqueous solution of methylene blue became colorless. The noticeable point was the best photocatalytic capability of iron oxide (Fe_2O_3) photocatalyst. XRD analysis displayed very small crystallite size of transition metal oxides. FE-SEM and EDX studies confirmed morphology and elemental compositions of the samples respectively. BET results revealed that iron oxide exhibit highest surface area and lowest particle size. The photodegradation potency can be enhanced positively by small crystallite and particle size, large surface area, wide band gap energy, and decrease recombination of charges onto the surface of photocatalyst. The percentage degradation of the prepared four samples was obtained in the order $Fe_2O_3 > Co_3O_4 > MnO_2 > ZnO$. In conclusion, the synthesized nano-sized materials especially iron oxide nano-photocatalysts could be auspicious applicant to degrade the waste constituents and has forthcoming applications in resolving pollution affairs of the environment and can play healthier part in the maintenance of green environment.

Acknowledgments

Authors are thankful to the Islamia University of Bahawalpur (Pakistan) and Higher Education Commission of Pakistan for financial support of this project through research grant no. 6276/Punjab/NRPU/ R&D/HEC/2016. Authors from King Saud University, sincerely appreciate the Deanship of Scientific Research, King Saud University Riyadh (Saudi Arabia) for their contribution through Research Group No: 1438-068. Dr. Sonia Zulfiqar is grateful to AUC-Cairo for STRC mini-grant and project SSE-CHEM-S.Z.-FY19-FY20-FY21-RG (119)-2018-Oct-01-17-53-22.

References

[1] M. Ghosh, K. Manoli, X. Shen, J. Wang, A.K. Ray, Solar photocatalytic degradation of caffeine with titanium dioxide and zinc oxide nanoparticles, J. Photochem. Photobiol., A, 377 (2019) 1–7.

[2] S. Prabhu, S. Megala, S. Harish, M. Navaneethan, P. Maadeswaran, S. Sohila, R. Ramesh, Enhanced photocatalytic activities of ZnO dumbbell/reduced graphene oxide nanocomposites for degradation of organic pollutants via efficient charge separation pathway, Appl. Surf. Sci., 487 (2019) 1279–1288.

[3] R. Koutavarapu, B. Babu, C.V. Reddy, I.N. Reddy, K.R. Reddy, M.C. Rao, T.M. Aminabhavi, M. Cho, D. Kim, J. Shim, ZnO nanosheets-decorated Bi_2WO_6 nanolayers as efficient photocatalysts for the removal of toxic environmental pollutants and photoelectrochemical solar water oxidation,

J. Environ. Manage., 265 (2020) 110504, doi: 10.1016/j.jenvman.2020.110504.

[4] M.M. Mohamed, M.A. Ghanem, M. Khairy, E. Naguib, N.H. Alotaibi, Zinc oxide incorporated carbon nanotubes or graphene oxide nanohybrids for enhanced sonophotocatalytic degradation of methylene blue dye, Appl. Surf. Sci., 487 (2019) 539–549.

[5] M.A. Islam, I. Ali, S.M.A. Karim, M.S. Hossain Firoz, A.-N. Chowdhury, D.W. Morton, M.J. Angove, Removal of dye from polluted water using novel nano manganese oxide-based materials, J. Water Process Eng., 32 (2019), doi: 10.1016/j.jwpe.2019.100911.

[6] F. Motahari, M.R. Mozdianfard, F. Soofivand, M. Salavati-Niasari, NiO nanostructures: synthesis, characterization and photocatalyst application in dye wastewater treatment, RSC Adv., 4 (2014) 27654–27660.

[7] Y.-L. Ge, Y.-F. Zhang, Y. Yang, S. Xie, Y. Liu, T. Maruyama, Z.-Y. Deng, X. Zhao, Enhanced adsorption and catalytic degradation of organic dyes by nanometer iron oxide anchored to single-wall carbon nanotubes, Appl. Surf. Sci., 488 (2019) 813–826.

[8] I. Fatimah, S.N. Amaliah, M.F. Andrian, T.P. Handayani, R. Nurillahi, N.I. Prakoso, W.P. Wicaksono, L. Chuenchom, Iron oxide nanoparticles supported on biogenic silica derived from bamboo leaf ash for rhodamine B photodegradation, Sustainable Chem. Pharm., 13 (2019) 100149, doi: 10.1016/j.scp.2019.100149.

[9] P. Basavarajappa, B. Seethya, N. Ganganagappa, K. Eshwaraswamy, R. Kakarla, Enhanced photocatalytic activity and biosensing of gadolinium substituted $BiFeO_3$ nanoparticles, ChemistrySelect, 3 (2018) 9025–9033.

[10] C. Ravi Dhas, R. Venkatesh, K. Jothivenkatachalam, A. Nithya, B. Suji Benjamin, A. Moses Ezhil Raj, K. Jeyadheepan, C. Sanjeeviraja, Visible light driven photocatalytic degradation of Rhodamine B and Direct Red using cobalt oxide nanoparticles, Ceram. Int., 41 (2015) 9301–9313.

[11] R. Ranjith, V. Renganathan, S.-M. Chen, N.S. Selvan, P.S. Rajam, Green synthesis of reduced graphene oxide supported TiO_2/Co_3O_4 nanocomposite for photocatalytic degradation of methylene blue and crystal violet, Ceram. Int., 45 (2019) 12926–12933.

[12] M. Harshiny, S. Aiswarya Devi, M. Matheswaran, Spiny amaranth leaf extract mediated iron oxide nanoparticles: biocidal photocatalytic propensity, stability, dissolubility and reusability, Biocatal. Agric., 21 (2019), doi: 10.1016/j.bcab.2019.101296.

[13] C.V. Reddy, I.N. Reddy, V.V.N. Harish, K.R. Reddy, N.P. Shetti, J. Shim, T.M. Aminabhavi, Efficient removal of toxic organic dyes and photoelectrochemical properties of iron-doped zirconia nanoparticles, Chemosphere, 239 (2020), doi: 10.1016/j.chemosphere.2019.124766.

[14] A. Fujishima, X. Zhang, D.A. Tryk, Heterogeneous photocatalysis: from water photolysis to applications in environmental cleanup, Int. J. Hydrogen Energy, 32 (2007) 2664–2672.

[15] R. Reddy, C. Reddy, M. Nadagouda, N. Shetti, T. Aminabhavi, Polymeric graphitic carbon nitride ($g-C_3N_4$)-based semiconducting nanostructured materials: synthesis methods, properties and photocatalytic applications, J. Environ. Manage., 238 (2019) 25–40, doi: 10.1016/j.jenvman.2019.02.075.

[16] Z. Maolin, S. Guoying, F. Jiamo, A. Taicheng, W. Xinming, H. Xiaohong, Novel preparation of nanosized $ZnO–SnO_2$ with high photocatalytic activity by homogeneous co-precipitation method, Mater. Lett., 59 (2005) 3641–3644.

[17] S.B. Kokane, S.R. Suryawanshi, R. Sasikala, M.A. More, S.D. Sartale, Architecture of 3D $ZnCo_2O_4$ marigold flowers: influence of annealing on cold emission and photocatalytic behavior, Mater. Chem. Phys., 194 (2017) 55–64.

[18] S. Yousaf, T. Kousar, M.B. Taj, P.O. Agboola, I. Shakir, M.F. Warsi, Synthesis and characterization of double heterojunction-graphene nano-hybrids for photocatalytic applications, Ceram. Int., 45 (2019) 17806–17817.

[19] I. Ghaffar, M.F. Warsi, M. Shahid, I. Shakir, Unprecedented photocatalytic activity of carbon coated/MoO_3 core–shell nanoheterostructurs under visible light irradiation, Physica E, 79 (2016) 1–7.

[20] N.L. Reddy, V.N. Rao, M. Vijayakumar, R. Santhosh, S. Anandan, M. Karthik, M.V. Shankar, K.R. Reddy, N.P. Shetti, M.N. Nadagouda, T.M. Aminabhavi, A review on frontiers in plasmonic nano-photocatalysts for hydrogen production, Int. J. Hydrogen Energy, 44 (2019) 10453–10472.

[21] R.K. Sharma, R. Ghose, Synthesis of Co_3O_4–ZnO mixed metal oxide nanoparticles by homogeneous precipitation method, J. Alloys Compd., 686 (2016) 64–73.

[22] W.S. Mohamed, A.M. Abu-Dief, Synthesis, characterization and photocatalysis enhancement of Eu_2O_3-ZnO mixed oxide nanoparticles, J. Phys. Chem. Solids, 116 (2018) 375–385.

[23] K. Zafar, M. Aadil, M.N. Shahi, H. Sabeeh, M.F. Nazar, M. Iqbal, M.A. Yousuf, Physical, structural and dielectric parameters evaluation of new $Mg_{1-x}Co_xNi_yFe_{2-y}O_4$ nano-ferrites synthesized via wet chemical approach, AAAFM Energy, 1 (2020) 36–44.

[24] S. Cho, K.-H. Lee, Formation of zinc aluminum mixed metal oxide nanostructures, J. Alloys Compd., 509 (2011) 8770–8778.

[25] I. Shakir, Z.A. Almutairi, Rational solution-assisted synthesis of copper sulfide nanoparticles for ultrahigh-rate electrochemical energy storage, AAAFM Energy, 1 (2020) 1–8.

[26] M.C. Toroker, D.K. Kanan, N. Alidoust, L.Y. Isseroff, P. Liao, E.A. Carter, First principles scheme to evaluate band edge positions in potential transition metal oxide photocatalysts and photoelectrodes, Phys. Chem., 13 (2011) 16644–16654.

[27] M. Batzill, Fundamental aspects of surface engineering of transition metal oxide photocatalysts, Energy Environ. Sci., 4 (2011) 3275–3286.

[28] Q. Ni, J. Ma, C. Fan, Y. Kong, M. Peng, S. Komarneni, Spinel-type cobalt-manganese oxide catalyst for degradation of Orange II using a novel heterogeneous photo-chemical catalysis system, Ceram. Int., 44 (2018) 19474–19480.

[29] J. Singh, A. Rathi, M. Rawat, V. Kumar, K.-H. Kim, The effect of manganese doping on structural, optical, and photocatalytic activity of zinc oxide nanoparticles, Composites, Part B, 166 (2019) 361–370.

[30] H. Lee, Y.-K. Park, S.-J. Kim, B.-H. Kim, S.-C. Jung, Titanium dioxide modification with cobalt oxide nanoparticles for photocatalysis, J. Ind. Eng. Chem., 32 (2015) 259–263.

[31] U. Nwankwo, R. Bucher, A.B.C. Ekwealor, S. Khamlich, M. Maaza, F.I. Ezema, Synthesis and characterizations of rutile-TiO_2 nanoparticles derived from chitin for potential photocatalytic applications, Vacuum, 161 (2019) 49–54.

[32] K.R. Reddy, K. Nakata, T. Ochiai, T. Murakami, D.A. Tryk, A. Fujishima, Nanofibrous TiO_2-core/conjugated polymer-sheath composites: synthesis, structural properties and photocatalytic activity, J. Nanosci. Nanotechnol., 10 (2010) 7951–7957.

[33] X. Dong, X. Wang, J. Wang, H. Song, X. Li, L. Wang, M.B. Chan-Park, C.M. Li, P. Chen, Synthesis of a MnO_2–graphene foam hybrid with controlled MnO_2 particle shape and its use as a supercapacitor electrode, Carbon, 50 (2012) 4865–4870.

[34] S. Vasantharaj, S. Sathiyavimal, P. Senthilkumar, F. Lewis Oscar, A. Pugazhendhi, Biosynthesis of iron oxide nanoparticles using leaf extract of *Ruellia tuberosa*: antimicrobial properties and their applications in photocatalytic degradation, J. Photochem. Photobiol., B, 192 (2019) 74–82.

[35] S. Haq, W. Rehman, M. Waseem, V. Meynen, S.U. Awan, S. Saeed, N. Iqbal, Fabrication of pure and moxifloxacin functionalized silver oxide nanoparticles for photocatalytic and antimicrobial activity, J. Photochem. Photobiol., B, 186 (2018) 116–124.

[36] M. Salavati-Niasari, Synthesis and characterization of host (nanodimensional pores of zeolite-Y)–guest [unsaturated 16-membered octaaza–macrocycle manganese(II), cobalt(II), nickel(II), copper(II), and zinc(II) complexes] nanocomposite materials, Chem. Lett., 34 (2005) 1444–1445.

[37] A. Bashiri Rezaie, M. Montazer, M. Mahmoudi Rad, Environmentally friendly low cost approach for nano copper oxide functionalization of cotton designed for antibacterial and photocatalytic applications, J. Cleaner Prod., 204 (2018) 425–436.

[38] P. Sangaiya, R. Jayaprakash, Tuning effect of Sn doping on structural, morphological, optical, electrical and photocatalytic

properties of iron oxide nanoparticles, Mater. Sci. Semicond. Process, 85 (2018) 40–51.

[39] Z. Cao, M. Qin, Y. Gu, B. Jia, P. Chen, X. Qu, Synthesis and characterization of Sn-doped hematite as visible light photocatalyst, Mater. Res. Bull., 77 (2016) 41–47.

[40] I. Bibi, N. Nazar, M. Iqbal, S. Kamal, H. Nawaz, S. Nouren, Y. Safa, K. Jilani, M. Sultan, S. Ata, F. Rehman, M. Abbas, Green and eco-friendly synthesis of cobalt-oxide nanoparticle: characterization and photo-catalytic activity, Adv. Powder Technol., 28 (2017) 2035–2043.

[41] J. Lu, H. Ali, J. Hurh, Y. Han, I. Batjikh, E.J. Rupa, G. Anandapadmanaban, J.K. Park, D.-C. Yang, The assessment of photocatalytic activity of zinc oxide nanoparticles from the roots of *Codonopsis lanceolata* synthesized by one-pot green synthesis method, Optik, 184 (2019) 82–89.

[42] T. Bhuyan, K. Mishra, M. Khanuja, R. Prasad, A. Varma, Biosynthesis of zinc oxide nanoparticles from *Azadirachta indica* for antibacterial and photocatalytic applications, Mater. Sci. Semicond. Process, 32 (2015) 55–61.

[43] X. He, R. Büchel, R. Figi, Y. Zhang, Y. Bahk, J. Ma, J. Wang, High-performance carbon/MnO_2 micromotors and their applications for pollutant removal, Chemosphere, 219 (2019) 427–435.

[44] E. Darezereshki, Synthesis of maghemite (γ-Fe_2O_3) nanoparticles by wet chemical method at room temperature, Mater. Lett., 64 (2010) 1471–1472.

[45] M. Sugantha, P.A. Ramakrishnan, A.M. Hermann, C.P. Warmsingh, D.S. Ginley, Nanostructured MnO_2 for Li batteries, Int. J. Hydrogen Energy, 28 (2003) 597–600.

[46] Z. Huang, Y. Zhao, H. Xu, J. Zhao, Surfactant-free synthesis, photocatalytic and electrochemical property study of Co_3O_4 nanoparticles, Mater. Res. Bull., 100 (2018) 83–90.

[47] D. Raoufi, Synthesis and microstructural properties of ZnO nanoparticles prepared by precipitation method, Renewable Energy, 50 (2013) 932–937.

[48] S. Wu, A. Sun, F. Zhai, J. Wang, W. Xu, Q. Zhang, A.A. Volinsky, Fe_3O_4 magnetic nanoparticles synthesis from tailings by ultrasonic chemical co-precipitation, Mater. Lett., 65 (2011) 1882–1884.

[49] C.-H. Wang, H.-C. Hsu, J.-H. Hu, High-energy asymmetric supercapacitor based on petal-shaped MnO_2 nanosheet and carbon nanotube-embedded polyacrylonitrile-based carbon nanofiber working at 2 V in aqueous neutral electrolyte, J. Power Sources, 249 (2014) 1–8.

[50] M. Kahouli, A. Barhoumi, A. Bouzid, A. Al-Hajry, S. Guermazi, Structural and optical properties of ZnO nanoparticles prepared by direct precipitation method, Superlattices Microstruct., 85 (2015) 7–23.

[51] A.L. Patterson, The Scherrer formula for X-ray particle size determination, Phys. Rev. Mater., 56 (1939) 978–982.

[52] A. Khorsand Zak, W.H.A. Majid, M. Ebrahimizadeh Abrishami, R. Yousefi, X-ray analysis of ZnO nanoparticles by Williamson-Hall and size-strain plot methods, Solid State Sci., 13 (2011) 251–256.

[53] H. Namduri, S. Nasrazadani, Quantitative analysis of iron oxides using Fourier transform infrared spectrophotometry, Corros. Sci., 50 (2008) 2493–2497.

[54] Y.-S. Li, J.S. Church, A.L. Woodhead, Infrared and Raman spectroscopic studies on iron oxide magnetic nano-particles and their surface modifications, J. Magn. Magn. Mater, 324 (2012) 1543–1550.

[55] A. Lassoued, B. Dkhil, A. Gadri, S. Ammar, Control of the shape and size of iron oxide (α-Fe_2O_3) nanoparticles synthesized through the chemical precipitation method, Results Phys., 7 (2017) 3007–3015.

[56] A. Lassoued, M.S. Lassoued, B. Dkhil, S. Ammar, A. Gadri, Synthesis, structural, morphological, optical and magnetic characterization of iron oxide (α-Fe_2O_3) nanoparticles by precipitation method: effect of varying the nature of precursor, Physica E, 97 (2018) 328–334.

[57] R.A. Bepari, P. Bharali, B.K. Das, Controlled synthesis of α- and γ-Fe_2O_3 nanoparticles via thermolysis of PVA gels and studies on α-Fe_2O_3 catalyzed styrene epoxidation, J. Saudi Chem. Soc., 21 (2017) S170–S178.

[58] D. Jaganyi, M. Altaf, I. Wekesa, Synthesis and characterization of whisker-shaped MnO_2 nanostructure at room temperature, Appl. Nanosci., 3 (2013) 329–333.

[59] A.K.M.A. Ullah, A.K.M.F. Kibria, M. Akter, M.N.I. Khan, M.A. Maksud, R.A. Jahan, S.H. Firoz, Synthesis of Mn_3O_4 nanoparticles via a facile gel formation route and study of their phase and structural transformation with distinct surface morphology upon heat treatment, J. Saudi Chem. Soc., 21 (2017) 830–836.

[60] S. Vijayakumar, A.K. Ponnalagi, S. Nagamuthu, G. Muralidharan, Microwave assisted synthesis of Co_3O_4 nanoparticles for high-performance supercapacitors, Electrochim. Acta, 106 (2013) 500–505.

[61] K.A.M. Ahmed, K. Huang, Formation of Mn_3O_4 nanobelts through the solvothermal process and their photocatalytic property, Arabian J. Chem., 12 (2019) 429–439.

[62] M. Sajjad, I. Ullah, M.I. Khan, J. Khan, M.Y. Khan, M.T. Qureshi, Structural and optical properties of pure and copper doped zinc oxide nanoparticles, Results Phys., 9 (2018) 1301–1309.

[63] S. Singhal, J. Kaur, T. Namgyal, R. Sharma, Cu-doped ZnO nanoparticles: synthesis, structural and electrical properties, Physica B, 407 (2012) 1223–1226.

[64] A. Becheri, M. Dürr, P. Lo Nostro, P. Baglioni, Synthesis and characterization of zinc oxide nanoparticles: application to textiles as UV-absorbers, J. Nanopart. Res., 10 (2008) 679–689.

[65] Q.-Y. Cai, J. Li, J. Ge, L. Zhang, Y.-L. Hu, Z.-H. Li, L.-B. Qu, A rapid fluorescence "switch-on" assay for glutathione detection by using carbon dots–MnO_2 nanocomposites, Biosens. Bioelectron., 72 (2015) 31–36.

[66] W. Li, X.Y. Cui, R. Zeng, G. Du, Z. Sun, R. Zheng, S. Ringer, S. Dou, Performance modulation of α-MnO_2 nanowires by crystal facet engineering, Sci. Rep., 5 (2015) 8987, doi: 10.1038/srep08987.

[67] A.K. Zak, R. Razali, W.H.A. Majid, M. Darroudi, Synthesis and characterization of a narrow size distribution of zinc oxide nanoparticles, Int. J. Nanomed., 6 (2011) 1399–1403.

[68] J. Tauc, Optical properties and electronic structure of amorphous Ge and Si, Mater. Res. Bull., 3 (1968) 37–46.

[69] Z.-Y. Tian, N. Bahlawane, V. Vannier, K. Kohse-Höinghaus, Structure sensitivity of propene oxidation over Co-Mn spinels, Proc. Combust. Inst., 34 (2013) 2261–2268.

[70] G. Wang, X. Shen, J. Horvat, B. Wang, H. Liu, D. Wexler, J. Yao, Hydrothermal synthesis and optical, magnetic, and supercapacitance properties of nanoporous cobalt oxide nanorods, J. Phys. Chem. C, 113 (2009) 4357–4361.

[71] N. Shaheen, M.A. Yousuf, I. Shakir, S. Zulfiqar, P.O. Agboola, M.F. Warsi, Wet chemical route synthesis of spinel oxide nano-catalysts for photocatalytic applications, Physica B, 580 (2020) 411820, doi: 10.1016/j.physb.2019.411820.

[72] M.I. Litter, Heterogeneous photocatalysis: transition metal ions in photocatalytic systems, Appl. Catal., 23 (1999) 89–114.

[73] C.V. Reddy, I.N. Reddy, K.R. Reddy, S. Jaesool, K. Yoo, Template-free synthesis of tetragonal Co-doped ZrO_2 nanoparticles for applications in electrochemical energy storage and water treatment, Electrochim. Acta, 317 (2019) 416–426.

[74] R. Abargues, J. Navarro, P.J. Rodríguez-Cantó, A. Maulu, J.F. Sánchez-Royo, J.P. Martínez-Pastor, Enhancing the photocatalytic properties of PbS QD solids: the ligand exchange approach, Nanoscale, 11 (2019) 1978–1987.

[75] P.S. Basavarajappa, S.B. Patil, N. Ganganagappa, K.R. Reddy, A.V. Raghu, C.V. Reddy, Recent progress in metal-doped TiO_2, non-metal doped/codoped TiO_2 and TiO_2 nanostructured hybrids for enhanced photocatalysis, Int. J. Hydrogen Energy, 45 (2020) 7764–7778.

[76] L. Haroune, M. Salaun, A. Ménard, C.Y. Legault, J.-P. Bellenger, Photocatalytic degradation of carbamazepine and three derivatives using TiO_2 and ZnO: effect of pH, ionic strength, and natural organic matter, Sci. Total Environ., 475 (2014) 16–22.

[77] T. Sauer, G. Cesconeto Neto, H.J. José, R.F.P.M. Moreira, Kinetics of photocatalytic degradation of reactive dyes in a TiO_2 slurry reactor, J. Photochem. Photobiol., A, 149 (2002) 147–154.

[78] A. Alkaim, A. Aljeboree, N.A. Alrazaq, S. Jaafer, F. Hussein, A.J. Lilo, Effect of pH on Adsorption and photocatalytic degradation efficiency of different catalysts on removal of methylene blue, Chem. Asian J., 26 (2014) 8445–8448.